Gas Dynamic Effects on Laser Cut Quality

Kai Chen, Y. Lawrence Yao, and **Vijay Modi,** Dept. of Mechanical Engineering, Columbia University, New York, New York, USA. ***E-mail:*** yly1@columbia.edu

Abstract

The presence of a gas jet plays an important role in laser cutting. Both the cutting efficiency and cut quality are very sensitive to gas pressure and nozzle standoff distance because of the complex nature of shock fronts and associated phenomena in a supersonic gas jet impinging on a workpiece. An idealized case is considered first, where the cut is assumed to be a circular hole directly underneath and concentric with the gas jet nozzle. A more realistic case of an axisymmetric nozzle impinging on a plate with a linear cut is considered next. Unlike the idealized case, the problem now is three-dimensional. Simple experiments to measure the through-kerf mass flow rate were carried out for both geometries. The two important forces exerted by the gas jet for melt ejection, namely, shear force and pressure gradient, show the same trend as that of the mass flow rate with varying gas pressure and standoff. The mass flow rate for the three-dimensional case shows the same behavior as that of the axisymmetric case, indicating the basic shock structures of the axisymmetric case are applicable to the real cutting cases. Laser cutting of mild steels under the corresponding conditions was performed, and the cut quality characterized by roughness, dross attachment, and recast layer thickness was analyzed. The deterioration of cut quality with the gas pressure and standoff is found to closely match reductions in through-kerf mass flow rate. It is thus verified that the shock structure of the gas jet and the associated mass flow rate have a direct impact on laser cutting as predicted.

Keywords: Gas Jet, Shock Structure, Laser Cutting, Quality

Nomenclature

A_h hole cross section area (mm²)
A_s slot cross section area (mm²)
B slot width (m)
D workpiece thickness (m)
d hole diameter (m)
F vector of x-directed fluxes
F_v viscous flux
G vector of r-directed fluxes
G_v viscous flux
H nozzle standoff distance (m)
L slot length (m)
m_h through-hole mass flow rate (kg/sec.)
m_s through-slot mass flow rate (kg/sec.)
M mach number
p static pressure (Pa)
p_0 total pressure (Pa)

P_e total gauge pressure at delivery nozzle exit (Pa)
r radial coordinate (m)
U average velocity inside hole (m/s)
u,v velocities in x and r directions (m/s)
x axial coordinate (m)
y distance normal to the wall (m)
ρ density of gas (kg/m³)
μ effective viscosity of gas (kg/(ms))
μ_m viscosity of melt (kg/(ms))
γ specific heat ratio
ν kinetic viscosity of gas (m²/s)
τ stress tensor
τ_{xr} shear stress (Pa)
τ_{xx} normal stress (Pa)
τ_{rr} normal stress (Pa)
τ_a average shear stress inside hole (Pa)
δr molten layer thickness (m)
δp pressure drop through hole

1. Introduction

Assist gas plays an important role in laser cutting in order to eject melt from the cutting front. The cutting efficiency and cut quality are strongly dependent on the effective organization of the gas jet. In industrial practice, convergent nozzles are commonly employed to direct a gas jet to the cut region of the workpiece. The operating pressure and the distance of the nozzle from the workpiece (standoff) are normally determined empirically in industrial practice. Pressure levels and large standoffs that deviate significantly can lead to poor and unrepeatable cut quality. For a convergent nozzle, the flow downstream of the nozzle exit becomes supersonic if the upstream total reservoir pressure is greater than 1.89 bar for air. This is typically the case in most laser cutting operations. The complex nature of the shock structure associated with the supersonic gas jet impinging on a workpiece can lead to unreliable behavior and poor cutting quality.

There are a number of experimental and theoretical investigations on the effects of the gas jet in laser cutting. However, most of the previous research efforts

have focused on the study of different nozzle designs. The performance of various supersonic nozzles was studied by Edler and Berger[1] and LaRocca et al.[2] The off-axis configuration in tandem with a coaxial one was investigated by Chryssolouris and Choi,[3] and the use of a single off-axis nozzle was studied experimentally by Brandt and Settles.[4] A buffer nozzle was designed to combat the effect of impurity caused by turbulent jet injection.[5] Little work has been performed to study the gas jet effects from the viewpoint of shock structure. The phenomena of the gas jet interacting with the cut kerf and the associated shock structures were studied by Makshev et al.[6] and by Brandt and Settles[4] through experiments involving scale models. An analytical analysis of gas dynamics in laser cutting/grooving was given by Farooq and Kar.[7] A comprehensive review of the gas jet effects on laser cutting was presented by Fieret et al.[8]

The study of the interactions between the gas jet and workpiece is of both theoretical and practical interest. Gas jets impinging on plates have been well studied, but gas jets impinging on plates with certain features such as holes or slots have not been studied in detail. Practically, such study will enable the systematic determination of the optimal operation conditions so as to obtain high cutting efficiency and good cut quality. In particular, prediction capabilities through numerical modeling for such interactions involving various process parameters will be invaluable. A complete model of all such interactions, however, is rather complex to be numerically modeled. A circular nozzle often found in laser cutting together with a slot of cut kerf on the workpiece renders the problem to be three-dimensional. Melt removal by the gas jet requires determination of a free surface between the gas jet and melt. It is therefore important to simplify the interactions without losing the essence for any modeling efforts to be fruitful.

Prior to this study, an axisymmetric case, that is, a gas jet impinging on a workpiece with a concentric through hole, was studied.[9] The melt was not considered based on the observation that it has little effect on the jet characteristic upstream of the workpiece. Measurement of the through-hole mass flow rate revealed the complex fluid flow phenomena, which were attributed to the shock structure change that were numerically determined in the same study. A summary thereof is given in Section 2.1.

The aforementioned study is extended to a nonaxisymmetric case, and supporting experimental evidence is obtained by cutting experiments in the current study. Experiments are conducted to measure mass flow rate through a slot rather than a concentric hole on the workpiece as in the earlier study. The phenomena almost identical to the axisymmetric case are observed, clearly indicating that the shock structure change determined for the axisymmetric case in the aforementioned study also takes place in the slot case. In addition, it is shown that shear force and pressure gradient, the two forces that eject the melt from the cut kerf, exhibit a similar behavior as the mass flow rate. This clearly links the shock structure change to cutting efficiency and quality, which is verified in actual cutting experiments.

2. Numerical and Experimental Investigation of Axisymmetric Case

2.1 Simulation Background

The current study is largely a continuation of the axisymmetric work by the same authors[9] mentioned in the previous section. A brief summary is given here. Computer simulation was carried out for the calculation domain shown in *Figure 1*. The flow is assumed to be governed by the steady compressible Reynolds-Averaged Navier-Stokes (RANS) equations. A commercial CFD code, RAMPANT, is used for the numerical simulation. A two-equation turbulence model based on RNG theory is utilized.[10] In axisymmetric coordinates, the RANS equations can be written as

$$\frac{\partial(F - F_v)}{\partial x} + \frac{\partial(G - G_v)}{\partial r} = 0 \qquad (1)$$

In the above form (F, G) and (F_v, G_v) represent the inviscid and viscous flux terms, respectively.

$$F = r\begin{bmatrix} \rho u \\ \rho u^2 + p \\ \rho uv \\ (\rho e + p)u \end{bmatrix}, \; G = r\begin{bmatrix} \rho v \\ \rho uv \\ \rho v^2 + p \\ (\rho e + p)v \end{bmatrix},$$

$$F_v = r\begin{bmatrix} 0 \\ \tau_{xx} \\ \tau_{xr} \\ u\tau_{xx} + v\tau_{xr} \end{bmatrix}, \; G_v = r\begin{bmatrix} 0 \\ \tau_{xr} \\ \tau_{rr} \\ u\tau_{rx} + v\tau_{rr} \end{bmatrix} \qquad (2)$$
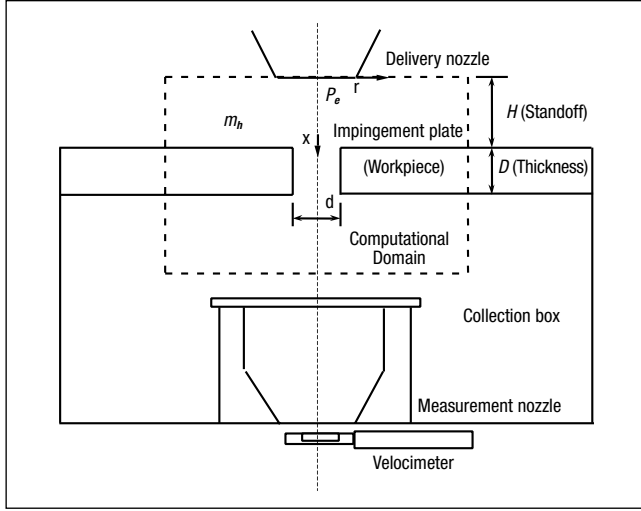
Figure 1
Schematic of Computational Domain and Experimental Setup for the Axisymmetric Case

where u and v are gas velocity in the x and r direction and p is the static pressure. The stress terms in axisymmetric coordinates are

$$\tau_{xx} = \mu[2\frac{\partial u}{\partial x} - \frac{2}{3}(\frac{1}{r}\frac{\partial}{\partial r}(rv) + \frac{\partial u}{\partial x})],$$

$$\tau_{rr} = \mu[2\frac{\partial v}{\partial r} - \frac{2}{3}(\frac{1}{r}\frac{\partial}{\partial r}(rv) + \frac{\partial u}{\partial x})], \quad (3)$$

$$\tau_{xr} = \tau_{rx} = \mu[\frac{\partial u}{\partial r} + \frac{\partial v}{\partial x}]$$

where τ_{xx} and τ_{rr} are normal stress, and τ_{rx} and τ_{xr} are shear stress. The effective viscosity μ is composed of the sum of molecular and turbulent contributions. To obtain μ, a two-equation turbulence model (RNG) is applied in addition to the momentum equations. The flow at the nozzle exit is assumed to be uniform and at sonic conditions. Sonic conditions are enforced at the nozzle lip by specifying the total pressure p_0 according to one-dimensional isentropic flow relations:

$$\frac{p_0}{p} = \left[1 + \frac{\gamma-1}{2}M^2\right]^{\frac{\gamma}{\gamma-1}} \quad (4)$$

where γ is the specific heat ratio. The mach number M is set to unity. At inlet boundaries the total pressure, static pressure, total temperature, and the flow direction are imposed. At the subsonic outlet boundary, the static pressure is specified, whereas the remaining flow properties are extrapolated. No-slip

wall and symmetry boundary conditions are applied at the plate and the centerline, respectively. The solver uses a semi-discrete finite-volume formulation, resulting in a consistent approximation to the conservation laws in integral form

$$\int_S [(F - F_v)dr - (G - G_v)dx] = 0 \quad (5)$$

For each iteration, RAMPANT solves the Navier-Stokes equations in integral form [Eq. (5)]. The equations are reduced to their finite-volume analogs by integrating over the computational cells into which the domain is divided.

2.2 Mass Flow Rate, Shear Force, and Pressure Gradient

Material removal during laser cutting takes place by the ejection of molten material. The melt ejection is a result of pressure gradient and the frictional force exerted by the gas jet. If the molten material is not efficiently ejected, the cut surface quality will deteriorate. It is thus very important to evaluate the shear force and pressure gradient inside the hole. The shear force and the pressure gradient are related with the through-hole mass flow rate. By definition, the total pressure consists of the static pressure and the velocity head:

$$p + \frac{1}{2}\rho(v^2 + u^2) = \frac{1}{2}\rho U^2 \quad (6)$$

where U is the characteristic velocity inside hole where the static pressure is chosen as reference pressure and is 0. A scaling analysis will give the pressure gradient as

$$\frac{\partial p}{\partial x} \propto -\frac{p_0}{d} = -\frac{1}{2}\frac{\rho U^2}{D} \quad (7)$$

where D is the thickness of the workpiece. The scaling of the shear stress can be obtained from Eq. (3):

$$\tau \propto \delta r \frac{\partial p}{\partial x} \propto \mu \frac{U}{\tau} \cdot \frac{\rho U^2}{D} \quad (8)$$

thus

$$\tau \propto (\frac{\mu\rho U^3}{D})^{\frac{1}{2}} \quad (9)$$

where δr is the thickness of the shear boundary. The through-hole mass flow rate is proportional to the gas velocity of U:
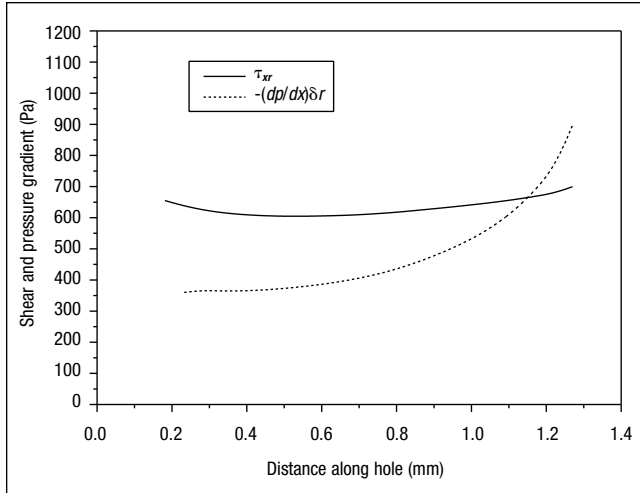
Figure 2
Shear Force and Pressure Gradient Effects Inside Hole
(P_e = 363 kPa, H = 1.5 mm, d = 0.508 mm)

Figure 3
Variation of Through-Hole Mass Flow Rate and Average Shear Force
Inside Hole with Total Gas Pressure (H = 2 mm)

$$m_h \propto \rho A U \tag{10}$$

where A is the cross section area of the hole. From the scaling analysis, it is seen that both shear force and pressure gradient are proportional to U, which is reflected in through-hole mass flow rate.

If the velocity profile of the molten material is assumed to be linear across the layer due to its extreme thinness, the velocity of the molten material can be calculated using the 1/7th power law of mean velocity profile,[11] that is

$$\frac{U}{v^*} = 8.74(\frac{dv^*}{2v})^{1/7} \tag{11}$$

$$\rho v^{*2} = \frac{\mu_m V}{\delta r} \tag{12}$$

where V is the surface velocity of the molten layer, v is the kinetic viscosity of the gas, δr is the thickness of the molten layer, and v^* is the friction velocity. However, the molten layer thickness is also dependent on the gas velocity as well as cutting speed.[12]

Through-hole mass flow rate with variation of standoff distance and gas pressure was calculated and measured in experiments. A simple experiment to measure the mass flow rate through the hole was designed to validate the simulation results (*Figure 1*). A collection box was placed directly underneath the workpiece to collect the flow and direct it to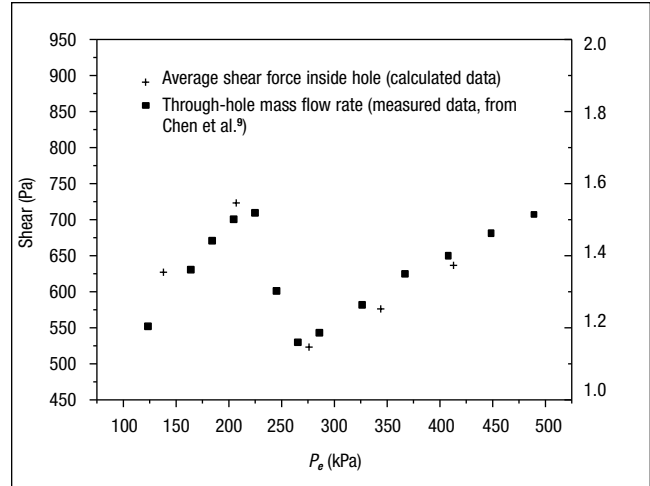 a measurement nozzle with a hole diameter much larger than the hole in workpiece. The gas velocity leaving the measurement nozzle is thus considerably reduced, permitting accurate measurement by a hot-film velocimeter.

Figure 2 shows typical calculated shear force and pressure gradient effects inside the hole. It should be noted that at the top and bottom edge of the hole, the shear force and the pressure gradient display divergences, which are caused by numerical errors due to abrupt changes in geometry. In comparing the effects of shear and pressure gradient, the shear layer is taken to be the thickness of the molten layer δr and is assumed to be of the order of 10^{-5} m, which is commonly reported.[2,6] For convenience, it is assumed that $\delta r = 2.0 \times 10^{-5}$ m and $D = 1.6$ mm. One then observes that the contributions of the shear force and the pressure gradient to the total force are of the same order. This is in agreement with the analysis given by Vicanek et al.[12]

Figure 3 shows the effect of gas pressure on the variation of average shear force inside the hole (τ_a) together with that of the through-hole mass flow rate. The shear force values close to either edges of the hole are assumed to be unreliable and hence not counted in the averaging procedure. τ_a follows the same pattern as m_h when P_e varies. The maximum τ_a corresponds to the maximum m_h, and the minimum τ_a corresponds to the minimum m_h, which confirms that the change of shear force due to the change of shock structure can be reflected by the change of through-hole mass flow rate. It was found that at large standoffs (H = 2 mm in this case), the through-
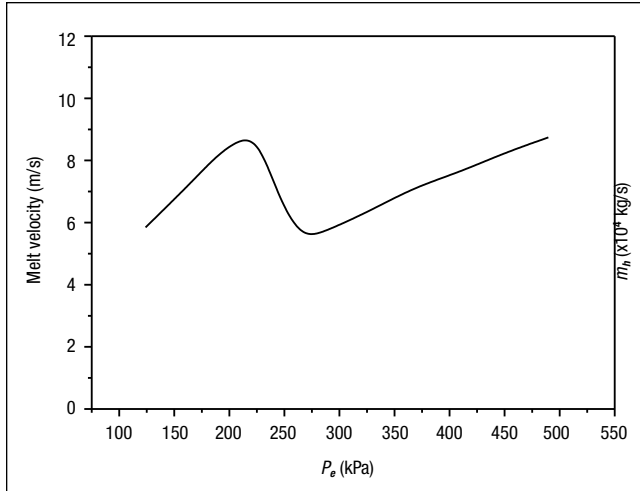
Figure 4
Variation of Average Melt Surface Velocity with Total Gas Pressure
(H = 2 mm)

Figure 5
Variation of Through-Hole Mass Flow Rate and Average Shear Force
Inside Hole with Standoff Distance (P_e = 363 kPa)

hole mass flow rate (m_h) does not monotonously increase with the gas pressure. Instead, it has a local maximum and minimum at certain pressure levels.

Figure 4 shows the calculated melt surface velocity versus gas pressure. The average surface velocity of the melt flow is derived from Eqs. (11) and (12). Again, it is assumed that the thickness of the molten layer has a fixed value $\delta r = 2.0 \times 10^{-5}$ m for convenience, although it may vary along the jet direction and is dependent on gas velocity and cutting speed. The average gas velocity inside the hole is obtained from the through-hole mass flow rate m_h. The other gas and melt properties are assumed to be constant, though they may vary with temperature:

$$\rho = 1.2 \text{ kg/m}^3, \qquad \nu = 2.25 \times 10^{-4} \text{ m}^2/\text{s},$$
$$\mu_m = 5 \times 10^{-3} \text{ kg/(ms)}, \qquad \delta r = 2.0 \times 10^{-5} \text{ m}$$

It is seen that the melt surface velocity shows the same patterns as that of the shear force and through-hole mass flow rate with the variation of the gas pressure.

The variation of shear force τ_a and through-hole mass flow rate m_h with standoff is shown in *Figure 5*. Again, τ_a and m_h exhibit a similar pattern as H varies while gas pressure P_e is fixed. If the gas pressure is held at a relatively high value (P_e = 363 kPa in this case), m_h is found to decrease continuously with increasing standoff until a critical value of the standoff where a sudden jump in m_h is observed. Similarly, the melt surface velocity with varying standoff can also be calculated and shows the similar patterns and the shear force and through-hole mass flow rate.
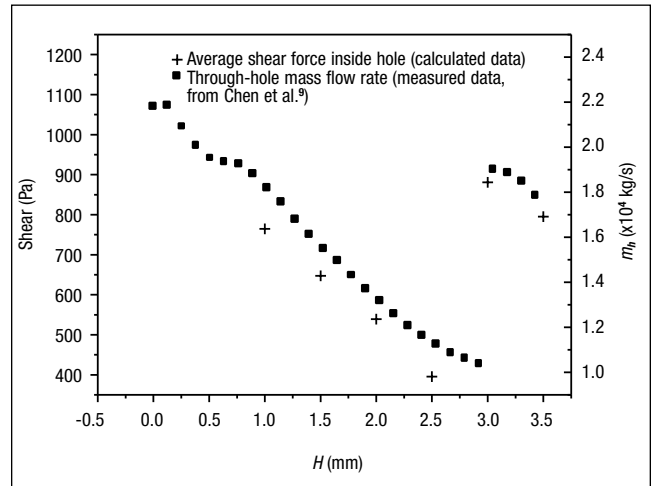
The above-described behaviors are essentially repeated for different hole sizes; specifically, there is a "bump" in m_h with increasing P_e while H is fixed at 2 mm, and a "jump" in m_h with increasing H while P_e is fixed at 363 kPa. It was determined that they are associated with changes in shock structure as gas pressure and standoff are varied, namely, the change of shock structure either from direct interaction between the oblique shock and the normal shock to indirect interaction, or vice versa.. At lower P_e values, the oblique shock waves meet at the centerline and are reflected prior to interacting with the normal shock (*Figure 6a*). In this case, the total pressure decrease downstream of the normal shock is small. At higher P_e values, the oblique shock interacts with the normal shock directly, resulting in a much larger total pressure reduction (*Figure 6b*). Thus, m_h may not always increase with P_e because of larger total pressure reduction across the normal shock. On the contrary, if P_e is fixed at a high level, the oblique shock will interact with the normal shock directly until H increases to a certain value where the oblique shock starts to merge first. This corresponds to a sudden jump in m_h at a certain H value.

The axisymmetric study reveals that contributions of shear force and pressure gradient are of the same order of magnitude and they follow the same profile as that of through-hole mass flow rate with the varying gas pressure and standoff. It is thus expected that under certain operating conditions when the mass flow rate is high, the shear force and pressure gradient are also large, the melt is better ejected in laser cutting,
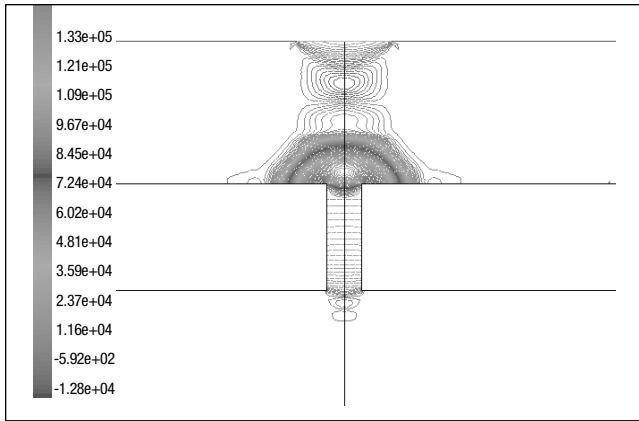
Figure 6a
Contour of Static Pressure (P_e = 138 kPa, d = 0.5 mm, H = 2 mm) in
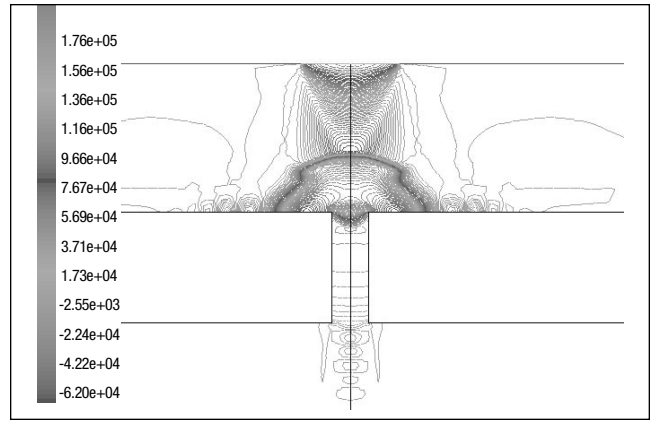Which Oblique Shock Merges Before Interacts with Normal Shock

Figure 6b
Contour of Static Pressure (P_e = 276 kPa, d = 0.5 mm, H = 2 mm) in
Which Oblique Shock Interacts with Normal Shock Directly

and the cut quality is relatively good. It will be shown in the subsequent sections that the generic behaviors of the gas flow between the real cutting case and that of this axisymmetric case are very similar.

3. Model Kerf Experiments

In laser cutting, the gas jet interacts with the work-piece to generate a narrow cut kerf. The cut kerf geometry renders the problem three-dimensional, leading to departure from axisymmetric behavior. To examine this departure, experiments were carried out by replacing the hole on the workpiece with a slot that attempts to capture the essential geometric feature of the real cut kerf. The mass flow rate through the slot was measured using the same collection box and measurement nozzle as that used in measuring the through-hole gas flow (*Figure 1*). The impingement plate (workpiece) along with the collection box are placed on a precision *x-y* table so that one end of the slot end can be adjusted to align with the delivery nozzle axis (*Figure 7*). The slot width (B) is set to be 0.22 mm, which equals the average kerf width in the subsequent real cutting experiments. Ideally, the slot length needs to be relatively long compared with the slot width, as in the case of a real cutting kerf. However, the ability of a collection box to function requires that the pressure drop for the flow through the collection box is negligible compared to the pressure drop through the kerf. Thus, as the slot length increases and the pressure drop through the kerf decreases, a point is reached where the collection box resistance may no longer be negligible, allowing gas flow entering the slot to begin to reemerge. It is
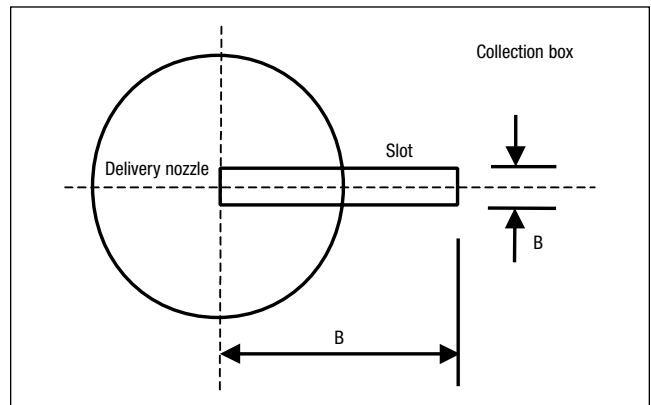

Figure 7
Top View of Model Kerf Experiment Setup

important to establish that the model kerf geometry does not reach such a point.

To establish this point, the variation in through-slot mass flow rate (m_s) with varying slot length (L) was measured for three different gas pressure levels, as shown in *Figure 8*. As seen, m_s first increases linearly with L, then levels off and eventually decreases as L exceeds about 1.8 mm. This decrease indicates reemergence of the gas flow from the collection box, thus invalidating the measurement. Hence, the slot length L was maintained at 1.1 mm to ensure accuracy in measurement, while at the same time L is five times larger than B, ensuring that the effect of the slot mimics a real cut kerf.

Figure 9 shows the effect of gas pressure on the through-slot (L = 1.1 mm) mass flow rate m_s for standoff distances H = 1.0, 1.5, and 2.0 mm. For H = 1.0 mm, m_s is found to monotonically and linearly increase with P_e. For H = 2.0 mm, however, m_s first increases with total pressure until it reaches a local
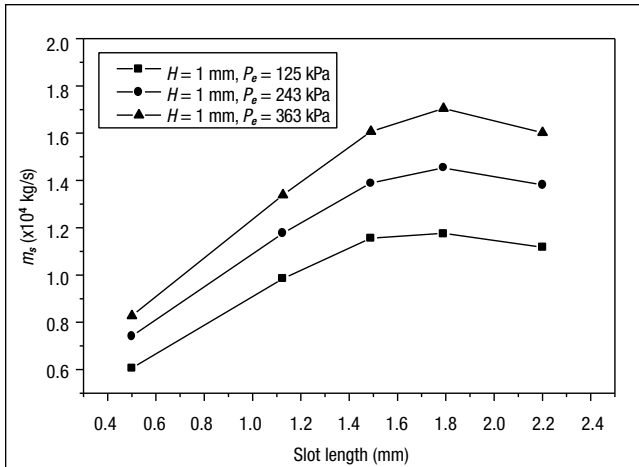
Figure 8
Variation of Measured Through-Slot Mass Flow Rate
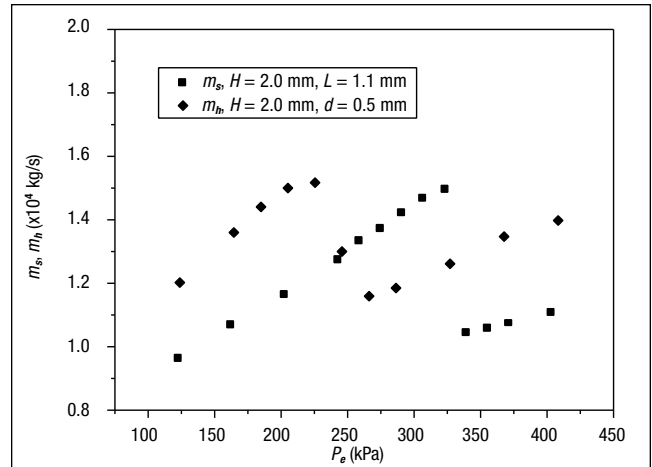**with Slot Length L**

Figure 10
Comparison of Through-Slot ($L = 1.1$ mm) and Through-Hole ($d = 0.5$
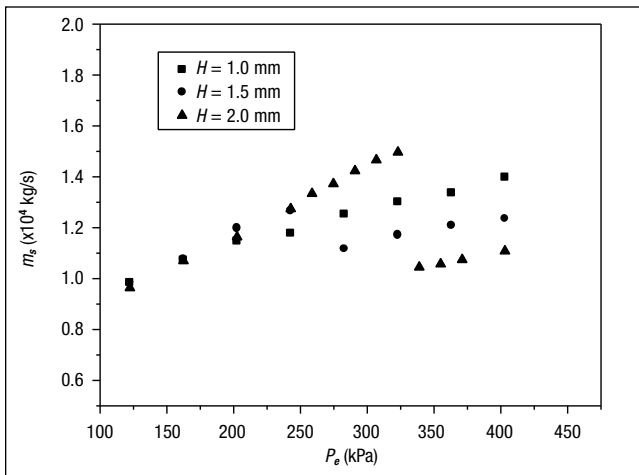**mm) Mass Flow Rate Measurements for $H = 2.0$ mm ($A_s \sim A_h$)**

Figure 9
Variation of Measured Through-Slot Mass Flow Rate Measurements
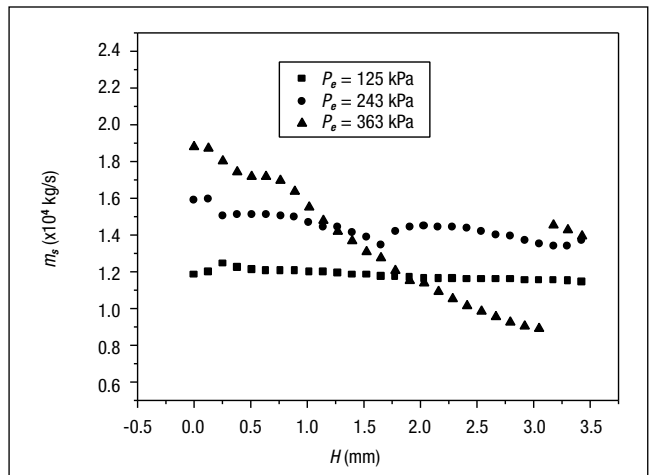**with Total Gas Pressure for $L = 1.1$ mm**

Figure 11
Variation of Through-Slot Mass Flow Rate Measurements with
Standoff Distance for $L = 1.1$ mm

maximum at $P_e = 325$ kPa and then reduces even as total gas pressure increases, until it reaches a local minimum and begins to increase again. For $H = 1.5$ mm, m_s behavior lies in between those of $H = 1.0$ mm and 2.0 mm, and the local maximum and minimum are not evident. These phenomena are similar to those of m_h behavior in the axisymmetric case. The "bump" in m_s with varying P_e for $H = 2.0$ mm is caused by the change of shock structure as explained in Section 2.

Comparing the behavior of m_s ($H = 2.0$ mm and $L = 1.1$ mm) and the behavior of m_h ($H = 2.0$ mm and $d = 0.5$ mm) of two cases with the same cross section area, it is seen that they resemble each other except that the "bump" shifts to high P_e values (*Figure 10*). This is probably due to the fact that an

edge of the slot is positioned at the center of the nozzle (*Figure 7*), causing less gas to enter the slot in comparison with the case of a concentric hole under the same pressure. The precise m_s behavior for a real cut kerf is likely to have a "bump" that shifts to lower P_e in comparison to the case of $L = 1.1$ mm because of more gas entering the slot.

The behavior of m_s ($L = 1.1$ mm) with varying standoff is shown in *Figure 11* for nozzle pressure P_e = 125, 243, and 363 kPa. At P_e values of 125 and 243 kPa, m_s is relatively unaltered with increasing H. For $P_e = 363$ kPa, m_s reduces continuously as H increases then suddenly jumps to a high value at a critical standoff. Again these phenomena are consistent with those of an axisymmetric case. The sudden

jump of m_s for $P_e = 363$ kPa is due to the change in shock structure, as explained in Section 2.

Figure 12 shows the comparison of the through-slot mass flow rate for $L = 1.1$ mm with the through-hole mass flow rate for $d = 0.5$ mm, both for a $P_e = 363$ kPa. Once again, the variations of m_s and m_h with varying standoff are very similar. They both show a sudden "jump" at about $H = 3.0$ mm. The fact that the m_h value is larger than the m_s value for the same H value is due to more gas entering the hole than entering the slot, as explained earlier.

The overall trends in both through-slot and through-hole mass flow rate with varying gas pressure and standoff are the same. This implies that the gas jet interaction with a slot-type cut kerf has a similar shock structure to that of a concentric hole. Because the cut kerf width is considerably smaller as compared with the exit diameter of the delivery nozzle, the kerf geometry has little influence on the shock structure upstream of the workpiece. The Schieren images of a geometry-scaled model kerf flow field provided by Brandt and Settles[4] show very similar shock patterns to those of axisymmetric cases as shown in *Figure 2*. It has been seen that the shear force and the pressure gradient have similar profiles as the mass flow rate with the variation of the gas pressure and standoff. It is reasonable to expect that the variation of the cut quality with varying gas pressure and standoff follows the same pattern of the variation of the through-slot mass flow rate. This is verified in the following section.

4. Laser Cutting Results and Discussion

To verify the gas jet effects on laser cut quality, laser cutting experiments were carried out under the same conditions as those of model kerf experiments. A PRC-1500 CO_2 laser with maximum output 1.5 kW, operated in CW and TEM_{00} modes was used for cutting experiments. The material being cut was cold-rolled mild steel of 1.6 mm thickness, which is the same thickness as the impingement plate in the through-hole and model kerf experiments for mass flow rate studies. In group-1 experiments, air was used as assist gas for cutting, the gas pressure P_e was fixed at 363 kPa, and the nozzle standoff distance H was varied. In group-2 experiments, oxygen was used for cutting, H was fixed at 2.0 mm, and P_e was varied from 122 kPa to 443 kPa, which is the typical pressure range for oxygen-assisted cutting of
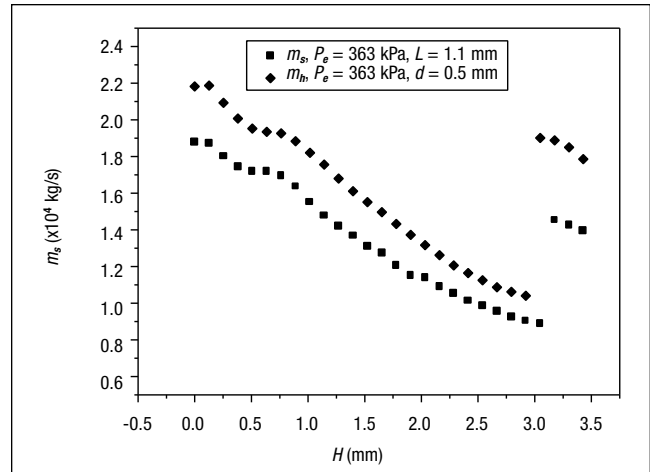
Figure 12
Comparison of Through-Slot ($L = 1.1$ mm) and Through-Hole ($d = 0.5$ mm) Mass Flow Rate Measurements for $H = 2.0$ mm ($A_s \widetilde{\ } A_h$)

mild steels. Each group consisted of two experimental runs under the same conditions. It should be noted that the pressure values read from a pressure meter were calibrated to the total gauge pressure at the nozzle exit, that is, P_e, by a relationship developed earlier.[9] These operating conditions given by gas pressure and standoff are identical to the conditions under which the through-slot and through-kerf mass flow rates were measured. To show their effects on cut quality most distinctively, the laser power and cutting speed were adjusted so that some samples were either barely cut through or not cut through at all. For group-1 experiments, the laser power and cutting speed were 800 W and 35 mm/s, respectively. For group-2 experiments, the laser power was set to 200 W and the cutting speed was set as 40 mm/s.

In group-1 experiments with air-assisted cutting, the less oxidized iron in the air-assisted cutting has much higher viscosity and surface tension than the oxide-rich melt in oxygen-assisted cutting,[13] and hence it is harder to eject the melt. Depending on the removal capability of the gas jet, resolidified melt (dross) may cling to the bottom edge of the cut kerf. It is expected that more dross will be attached to the edge when the ejecting force exerted by the gas jet is weak, and vice versa. *Figure 13* shows the dross attachment on cut edge with four different standoffs in the first run of the experiments. Dross was observed at $H = 1.0$ mm. The amount of dross increases for $H = 1.5$ mm. Cuts were incomplete at $H = 2.0$ and 2.5 mm, which is equivalent to extremely severe dross attachment. The dross attachment then suddenly decreases to a minimum amount at $H = 3.0$ mm, and it increases slightly at $H = 3.5$ mm. If the variation of dross attachment with standoff is com-
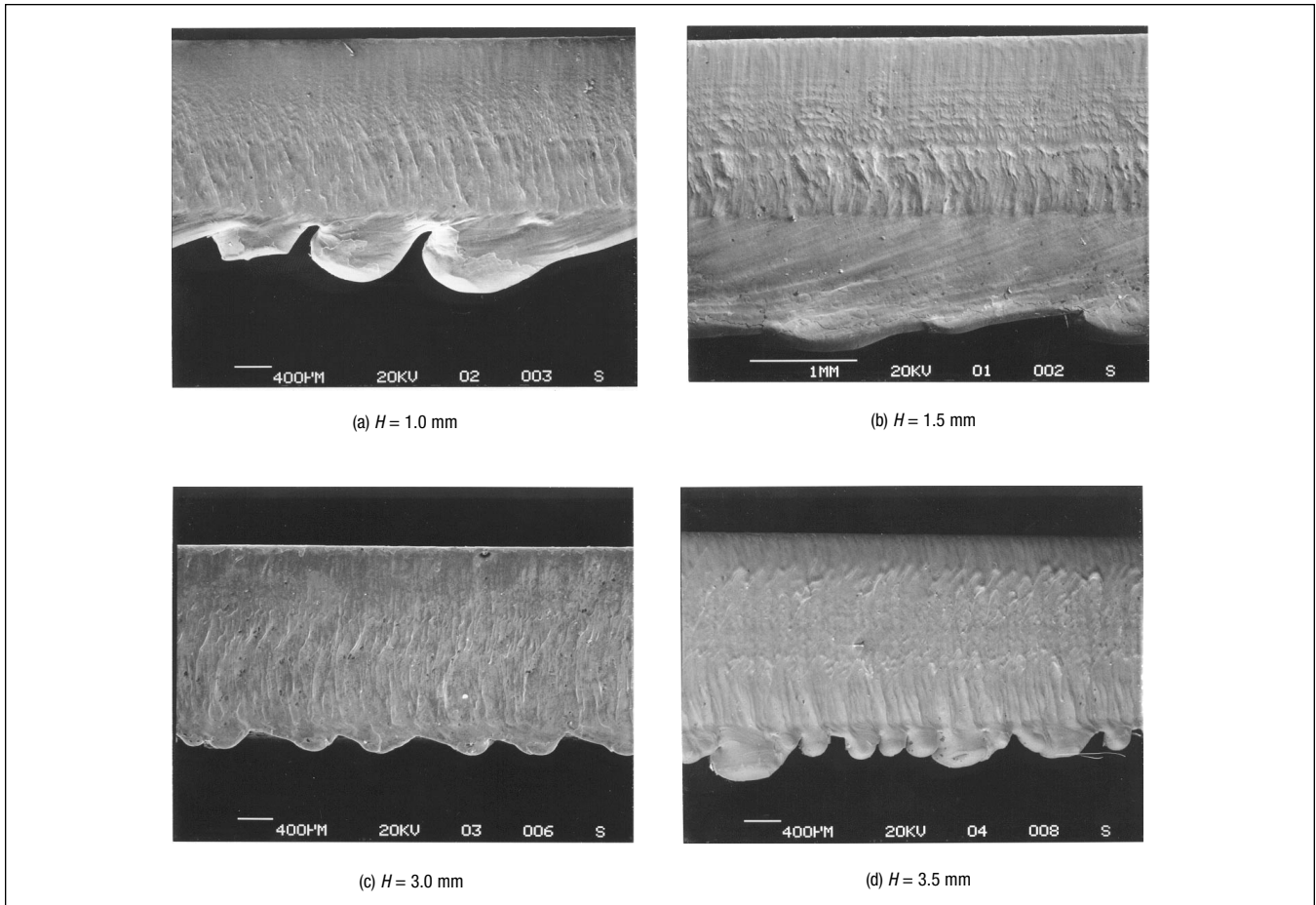
(a) *H* = 1.0 mm

(b) *H* = 1.5 mm

(c) *H* = 3.0 mm

(d) *H* = 3.5 mm

Figure 13
SEM of Dross Attachment on Cut Surface with Different Standoff at P_e = 363 kPa (laser power: 800 W; cutting speed: 35 mm/s; material thickness: 1.6 mm; air assisted; incomplete cuts for *H* - 2.0 and 2.5 mm)

pared with the variation of through-slot mass flow rate shown in *Figure 12*, it is seen that they exhibit opposite patterns. The sudden decrease in the dross corresponds to the jump of the through-hole mass flow rate. It is easy to understand this correspondence because the through-kerf mass flow rate has similar trends as the shear stress and pressure gradient (*Figure 4*), the two forces responsible for melt removal. At the same time, the interesting pattern of change in the through-slot mass flow rate with total gas pressure P_e and standoff *H* has been attributed to the change in the shock structure upstream of the workpiece. So this study fundamentally explains why the total gas pressure and standoff have direct impact on the cut quality.

Each cut kerf in group-1 experiments was cross-sectioned and examined under SEM. Because of higher viscosity and surface tension associated with unoxidized molten iron, it is normally not all ejected from the cut zone in such inert-gas assisted cutting. The melt not ejected from the cut zone will resolidify on the cut sur-

face and form a recast layer. The thickness of the recast layer varies depending on the removal capability of the gas jet—the larger the removal capability, the thinner the recast layer, and vice versa. *Figure 14* shows SEM pictures of the recast layer on the surface of the cut kerf of each sample from the second run. The recast layer increases as *H* increases from 1.0 to 1.5 mm, then decreases to a minimum value at *H* = 3.0 mm, and again increases slightly at *H* = 3.5 mm. If the cases of incomplete cuts at *H* = 2.0 and 2.5 mm are considered to be equivalent to the maximum recast layer, the pattern of change of the recast layer thickness with standoff is similar to that of dross attachment. Note that, contrary to oxygen-assisted cutting, there is no evident stria on the cut kerf because air was used as the assist gas.

In group-2 experiments, the samples were not cut through for P_e = 323 kPa, 363 kPa in the first run, and for P_e = 122 kPa, 363 kPa of the second run. To quantify the surface roughness, measurements were taken using a profilometer along a line 0.4 mm from the bot-
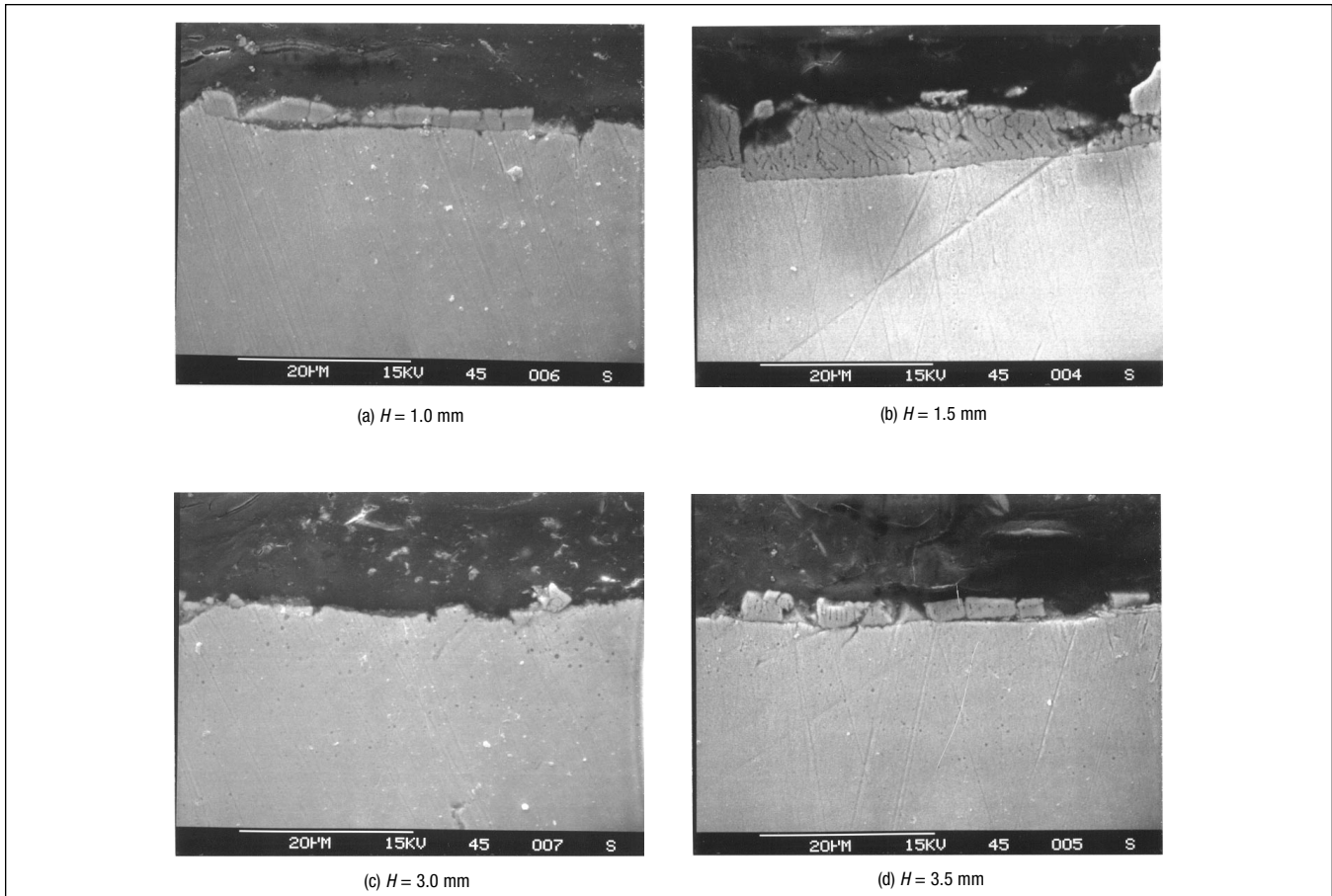
(a) $H = 1.0$ mm

(b) $H = 1.5$ mm

(c) $H = 3.0$ mm

(d) $H = 3.5$ mm

Figure 14
SEM of Recast Layer on Cut Surface with Different Standoff at P_e = 363 kPa (laser power: 800 W; cutting speed: 35 mm/s;
material thickness: 1.6 mm; air assisted; incomplete cuts for H - 2.0 and 2.5 mm)

tom. SEM pictures of the cut kerf from the second run, as well as their profilometer traces at three different gas pressure levels, are shown in *Figure 15*. On the upper portion of the cut kerf, regular stria are seen. Their formation involves more complicated physics and is studied by many researchers.[14] On the lower portion of the cut kerf, surface finish becomes rougher and less regular, and there is a small amount of dross attached along the bottom edge, which indicates the melt is ejected from there. The surface finish of the lower portion is therefore more directly influenced by the ejecting forces of shear and pressure gradient associated with the gas jet. As seen, the surface finish at P_e = 283 kPa is better than that at P_e = 162 kPa and P_e = 403 kPa. In fact, the best surface finish at the lower portion of the cut corresponds to a local maximum of the through-slot mass flow rate, as indicated in *Figure 10*, and a maximum of the shear and the pressure gradient (*Figure 4*).

Figure 16 shows the roughness R_a (root-mean-square average) of the lower portion of the cut vs. gas pressure

at standoff $H = 2.0$ mm. It also shows the through-slot mass flow rate measurement. The situations where cuts are incomplete are marked with a triangle at the top of the figure to indicate they correspond to the maximum roughness. As seen, the roughness decreases as P_e increases to about 300 kPa, before the cut becomes incomplete at P_e = 323 kPa; R_a then decreases again as P_e increases further. Comparing the variation of the roughness with the variation of the through-slot mass flow rate shown in the same figure, it is seen that the roughness follows a trend opposite to that of the through-slot mass flow rate. Please note that the P_e value corresponding to the maximum value of m_s for a real cut kerf should be slightly less than the P_e value of a limited slot length shown in *Figure 16*, as explained in Section 3. In other words, when one interprets the m_s curve in *Figure 16*, the curve should be slightly shifted to the left. With that in mind, the minimum value of roughness around P_e = 280 kPa will correspond to the maximum value of m_s, while incomplete cuts at P_e =
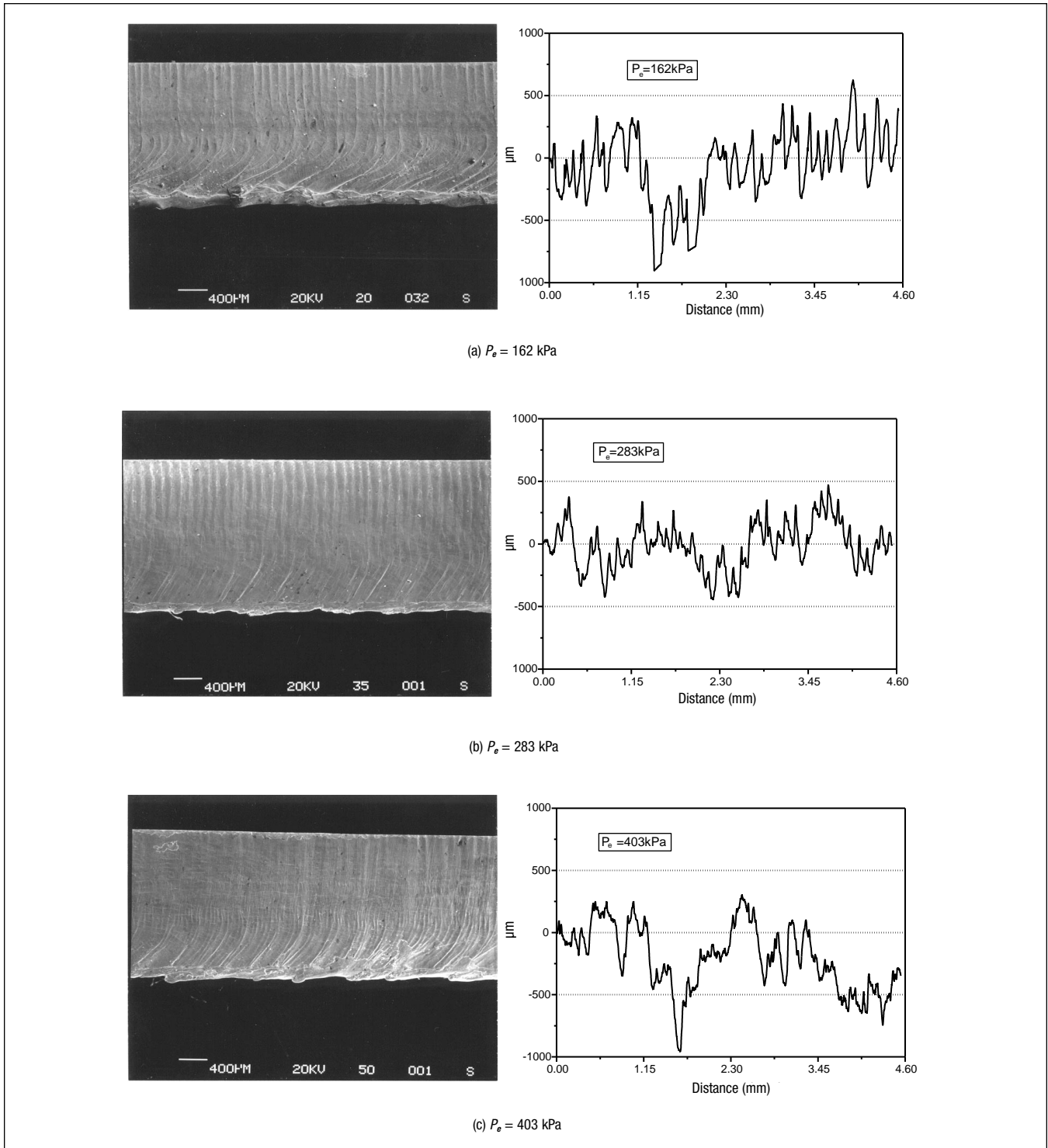
(a) P_e = 162 kPa

(b) P_e = 283 kPa

(c) P_e = 403 kPa

Figure 15
SEM and Profilometer Measurements of Cut Surface with Different Gas Pressure at 2.0 mm Standoff (laser power: 200 W; cutting speed: 40 mm/s; material thickness: 1.6 mm; oxygen assisted; incomplete cuts at P_e = 323 kPa, P_e = 363 kPa)

325 kPa correspond to the trough of the m_s curve. It is thus seen that a higher through-kerf mass flow rate corresponding to higher shear stress and pressure gradient results in better surface finish, whereas a lower through-kerf mass flow rate gives poor cut quality. The sudden drop of the mass flow rate with gas pressure for a standoff of $H = 2$ mm is due to the aforementioned change of the shock structures upstream of the workpiece.
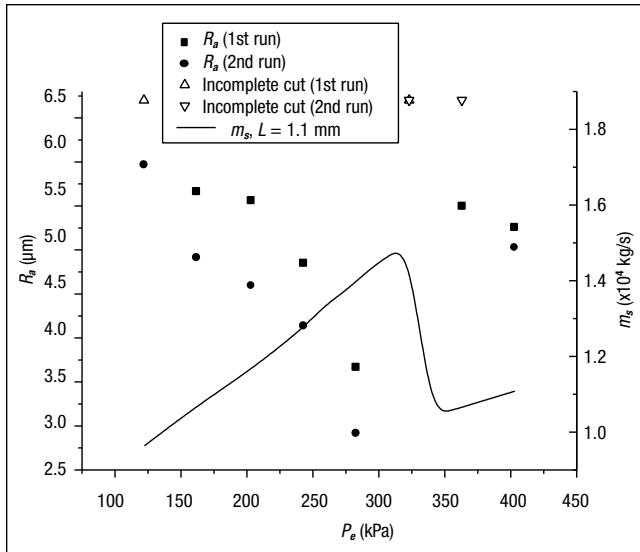
Figure 16
Roughness (R_a) Measurement at Low Portion of Cut Surface and Through-Slot Mass Flow Rate Measurement with Different Gas Pressure at H = 2.0 mm (laser power: 200 W; cutting speed: 40 mm/s; material thickness: 1.6 mm; oxygen assisted)

The experimental results show that the cut quality, including roughness, dross, and recast layer, vary with total gas pressure and standoff in a way strongly consistent with the pattern of change in the through-slot mass flow rate, which is in turn similar to the pattern of change in the through-hole mass flow rate. The pattern of change in through-hole mass flow rate has been attributed to the changes in shock structure as evidenced in the axisymmetric simulation. Although the interactions between laser and melt are not taken into account when the shock structures are predicted in the numerical simulation under the assumption that such interactions have insignificant effects on the shock structures upstream of the workpiece, this study shows that the primary behavior of shock structure in laser cutting is very similar to that in the axisymmetric case and that it directly influences the cut quality.

5. Conclusions

The effects of a gas jet in laser cutting are examined. It is found that the removal capability of the gas jet, in terms of shear stress and pressure gradient, is affected by the shock structure of the impinging jet interacting with the workpiece. The through-hole or through-slot mass flow rate is found to be a key indicator of shock structure and removal capability of the gas jet. When an oblique shock directly interacts with the normal shock, a large reduction in mass flow rate is observed. However, when an oblique shock merges upstream of its interaction with the normal shock, the reduction of the mass flow rate is small, preserving the removal capability. The variation of measured through-slot mass flow rate with gas pressure and standoff distance is similar to that of the through-hole mass flow (axisymmetric case), indicating that the basic shock structure of the two cases remains unchanged. Experimental measurement of cut quality characteristics such as roughness, dross attachment, and recast layer thickness confirms their association with the shock structure and gas jet removal capability as predicted.

Acknowledgment

References

1. R. Edler and P. Berger, "New Nozzle Concept for Cutting with High Power Lasers," Proc. of ICALEO'91, Orlando, FL, 1991, Laser Institute of America, pp253-262.

2. A.V. LaRocca et al., "Nozzle Design to Control Fluid-Dynamic Effects in Laser Cutting," SPIE (v2207, 1994), pp169-180.

3. G. Chryssolouris and W.C. Choi, "Gas Jet Effects on Laser Cutting," SPIE CO2 Lasers and Applications (v1042, 1989), pp86-96.

4. A.D. Brandt and G.S. Settles, "Effect of Nozzle Orientation on the Gas Dynamics of Inert-Gas Laser Cutting of Mild Steel," Journal of Laser Application (v9, 1997), pp269-277.

5. W. O'Neill and J.T. Gabzdyl, "The Mass Transfer Behaviour of Gas Jets in Laser Cutting," Welding in the World (v15, n1, 1995), pp6-11.

6. N.K. Makashev et al., "Gas Hydrodynamics of CW Laser Cutting of Metals in Inert Gas," SPIE (v2257, 1994), pp2-9.

7. K. Farooq and A. Kar, "Removal of Laser-Melted Material with an Assist Gas," Journal of Applied Physics (v83, n12, June 1998).

8. J. Fieret et al., "Overview of Flow Dynamics in Gas-Assisted Laser Cutting," SPIE High Power Lasers (v801, 1987), pp243-250.

9. K. Chen, Y.L. Yao, and V. Modi, "Numerical Simulation of the Gas Jet Effects in Laser Machining," Proc. of ICALEO'98, Section B, Orlando, FL, 1998, Laser Institute of America, pp120-129.

10. V. Yakhot and S.A. Orszag, "Renormalization Group Analysis of Turbulence - I. Basic Theory," Journal of Scientific Computing (v1, n1, 1986), pp3-51.

11. H. Schlichting, Boundary-Layer Theory (New York: McGraw-Hill Book Co., 1979).

12. M. Vicanek et al., "Hydrodynamic Instability of Melt Flow in Laser Cutting," Journal of Physics D: Applied. Physics (v20, 1986), pp140-145.

13. A. Ivarson et al., "The Oxidation Dynamics of Laser Cutting of Mild Steel and the Generation of Striations on the Cut Edge," Journal of Materials Processing Technology (v40, 1994), pp359-374.

14. K. Chen and Y.L. Yao, "Striation Formation and Melt Removal in the Laser Cutting Process," Journal of Mfg. Processes (v1, n1, 1999), pp43-53.

Authors' Biographies

Dr. Kai Chen was a PhD candidate and is currently with Unplugin, Inc., a software company in New York City. Dr. Y. Lawrence Yao is an associate professor with research interests in manufacturing and design, laser machining, laser forming, and laser shock processing. Dr. Vijay Modi is a professor with research interests in thermo-fluid science, CFD, microfluidics, MEMS, sensors, and optimal design.